Matter

CellPress

Article

Revealing the Origin of Improved Reversible Capacity of Dual-Shell Bismuth Boxes Anode for Potassium-Ion Batteries

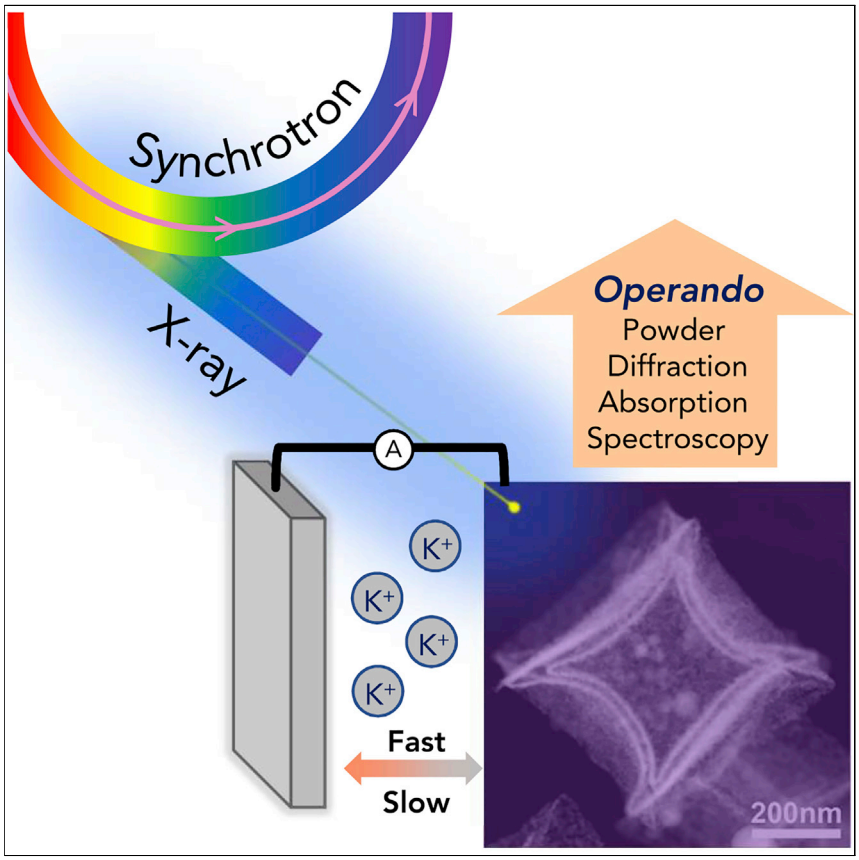

A significant improvement in reversible capacity was achieved for nanostructured alloy anodes. However, the origin of their improved reversible capacity remains unclear. Here, we combine several synchrotron-based X-ray techniques to study the double-shell nanostructured bismuth boxes to reveal the origin of their improved reversible capacity. These findings have the potential to serve as guidance for the rational design and engineering of electrode materials for various batteries.

Fangxi Xie, Lei Zhang, Biao Chen, ..., Bernt Johannessen, Mietek Jaroniec, Shi-Zhang Qiao

s.qiao@adelaide.edu.au

HIGHLIGHTS

The first synthesis of double-shell nanostructured bismuth boxes

The applications of various synchrotron-based X-ray characterizations

Revealing origins of the improved capacities at various current densities

3 **Understanding**
Dependency and conditional studies on material behavior

Xie et al., Matter 1, 1681–1693
December 4, 2019
Published by Elsevier Inc.
https://doi.org/10.1016/j.matt.2019.07.006

Matter

CellPress

Article

Revealing the Origin of Improved Reversible Capacity of Dual-Shell Bismuth Boxes Anode for Potassium-Ion Batteries

Fangxi Xie,[1,4] Lei Zhang,[1,4] Biao Chen,[1] Dongliang Chao,[1] Qinfen Gu,[2] Bernt Johannessen,[2] Mietek Jaroniec,[3] and Shi-Zhang Qiao[1,5,*]

SUMMARY

Nanostructured alloy anodes have been successfully used in several kinds of rocking-chair batteries. However, a full picture of the origin of their improved reversible capacity remains elusive. Here, we combine *operando* synchrotron-based X-ray powder diffraction and *ex situ* X-ray absorption near-edge structure spectroscopy to study the double-shell structured bismuth boxes as anodes in potassium-ion batteries to reveal the origin of their improved capacity. The nanostructured bismuth anode offers an enhanced capability to tolerate the volume expansion under a low current density of 0.2 C, resulting in a more complete alloy reaction. Additionally, under a high current density of 2 C, nanostructured bismuth anode with larger surface area offers more sites to electrochemically alloy with potassium and results in a lower average oxidation state of bismuth. These findings offer guidance for the rational design and engineering of electrode materials according to the current density for rocking-chair batteries.

INTRODUCTION

Rocking-chair batteries, such as lithium-, sodium-, potassium-, and calcium-ion batteries, are widely applied as electrical energy-storage devices for portable electronic devices and electrical vehicles. On their anode side, alloy anodes with much higher theoretical capacity than the conventional intercalation anodes are considered as a superior choice.[1–12] Nonetheless, these alloy anodes often suffer larger volume expansion and, consequently, capacity fading.[5–7,9] Therefore, various nanostructured alloy anodes have been developed.[3,4,9] Although a significant improvement in their reversible capacity has been achieved, its origin remains still unclear.[6,7]

Various approaches have been explored to reveal the origin of the improved capacity. The most common approach involves X-ray powder diffraction (XRPD) to observe the electrochemical alloying process. In particular, the previous studies involving the XRPD monitoring of the alloying process of silicon anodes in lithium-ion batteries suggest that the reduction of the particle size or film thickness leads to suppression of the $Li_{15}Si_4$ phase, which results in a change in electrochemical reaction and increases the reversible capacity of the final product.[7,13,14] Additionally, the final product of the alloying reaction of bismuth, another alloy anode, in sodium-ion batteries is affected by varying the particle size. The final product derived from nanosized bismuth and sodium is cubic Na_3Bi, while the one originating from microsized bismuth is hexagonal Na_3Bi.[15] The change in the electrochemical reaction path due to nanosizing the alloy anodes could be the reason for the improved reversible

Progress and Potential

A significant improvement in the reversible capacity was achieved for nanostructured alloy anodes. However, even though a large amount of nanostructured alloy anodes were applied in rocking-chair batteries, due to the limitation of lab-based techniques, the origin of their improved reversible capacity remains unclear. Here, we combine *operando* synchrotron-based X-ray powder diffraction with high temporal resolution and *ex situ* X-ray absorption near-edge structure spectroscopy to study the double-shell nanostructured bismuth boxes as alloy anodes for potassium-ion batteries to reveal the origin of their improved reversible capacity. Our results reveal that the origin under low current density is the change of electrochemical path while the one under high current density is the promotion of the surface-driven electrochemical reactions. These findings have the potential to serve as guidance for the rational design and engineering of nanostructured alloy anodes.

capacity.[7,15,16] However, most of the reported results refer to the electrochemical reaction paths under small current density. The difference in the behavior of nanostructured and bulky alloy anodes under high current density remains elusive due to the poor temporal resolution of lab-sourced XRPD, which might require a relatively long acquisition time for obtaining proper crystallographic information.[17–20] To resolve this issue, electrochemical characterization approaches with high temporal resolution have been applied. Several reports about anodes that contain alloy elements suggest that the origins of higher reversible capacity are the enhanced pseudocapacitive response or fast ion kinetics.[21–25] However, the characterization of electrochemical reactions is based mainly on the electrical signals while the information about chemical properties, such as the phase evolution or the oxidation states, is lacking. More importantly, the conclusion about the enhanced pseudocapacitive contribution is in contradiction with the suppression of certain electrochemical reactions observed by XRPD. At present, most of the reports are devoted to either the phase evolution under low current density or the electrochemical response under high current density. Therefore, due to the rarely reported phase evolution of nanostructured alloy anodes under high current density and the lack of chemical properties from electrochemical characterization, a full picture of the origin of increasing reversible capacity of nanostructured alloy anodes remains unclear.

Among several kinds of rocking-chair batteries, due to the abundance of potassium and its more negative voltage than that of sodium, potassium-ion batteries are considered as alternatives with higher energy density than that of sodium-ion batteries but smaller cost compared with lithium-ion batteries.[12,26,27] However, the first-principles density functional theory (DFT) study indicates larger volume expansion upon alloying with potassium than that upon alloying with sodium and lithium.[26] Development and application of nanostructured alloy anodes for potassium-ion batteries and their better understanding are more urgent issues than is the case for lithium- and sodium-ion batteries.

Herein, we report the first synthesis of double-shell structured bismuth boxes. Their electrochemical process as an anode for potassium-ion batteries is studied by combining an *operando* synchrotron-based XRPD with high temporal resolution and *ex situ* X-ray absorption near-edge structure (XANES).[17,19,20] By employing this nanostructured bismuth material and comparing its electrochemical behavior with that of microsized bismuth, a full picture of the origin of the improved reversible capacity of nanostructured alloy anodes is revealed. The improved reversible capacity of nanostructured bismuth under low current density originates from numerous internal voids able to accommodate the large volume expansion, while that under high current density originates from a large number of electrochemical active sites associated with high surface area. This study points out that the origins of the improved reversible capacities under various current densities are different, and demonstrates the key role of the nanostructure in improving the reversible capacity of alloy anodes. These findings offer guidance for the future rational design and engineering of nanostructured alloy anodes for rocking-chair batteries.

RESULTS AND DISCUSSION

The complete synthesis route of nanostructured bismuth anodes is illustrated in Figure 1A. As shown in Figures 1A and S1, the uniform ZIF-8 (zeolitic imidazolate framework-8) cubes with a size of around 500 nm were selected as the initial template and synthesized by using a slightly modified approach reported elsewhere.[28–31] It has been reported elsewhere that zinc sulfide can be turned into other sulfides through

[1]School of Chemical Engineering and Advanced Materials, The University of Adelaide, Adelaide, SA 5005, Australia

[2]Australian Synchrotron (ANSTO), 800 Blackburn Road, Clayton, VIC 3168, Australia

[3]Department of Chemistry and Biochemistry, Kent State University, Kent, OH 44242, USA

[4]These authors contributed equally

[5]Lead Contact

*Correspondence: s.qiao@adelaide.edu.au

https://doi.org/10.1016/j.matt.2019.07.006

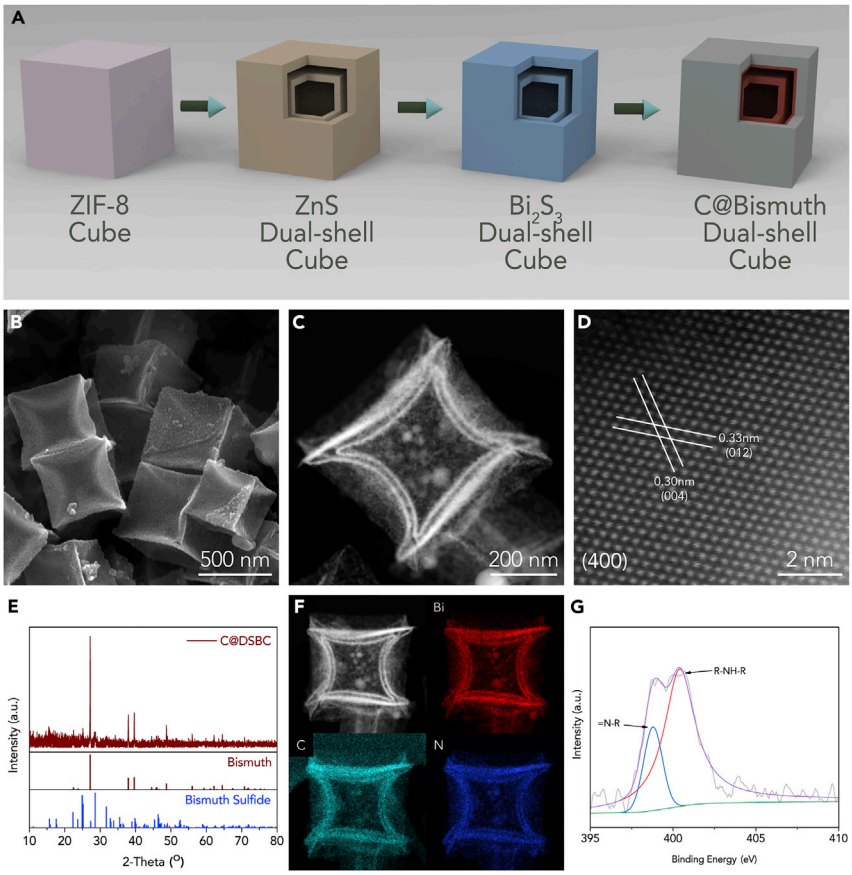

Figure 1. Synthesis Procedure, Morphology, and Physicochemical Characterization of C@DSBC

(A) Scheme illustrating the synthetic procedure of C@DSBC.

(B) SEM image of C@DSBC.

(C and D) HAADF-STEM images.

(E) XRPD spectrum with the standard patterns of bismuth and bismuth sulfide shown separately.

(F) HAADF-STEM elemental mapping.

(G) High-resolution nitrogen XPS spectrum.

this strategy.[29–33] After a series of modified sulfidations reported by us previously, the amorphous double-shell zinc sulfide boxes with slight indentations on their surface are clearly seen (Figures S2–S5).[32] As suggested in our previous report, due to the difference in the solubility product constants, the zinc cations in the as-prepared sample are replaced by bismuth cations via a facile room-temperature cation-exchange method (Figure S6).[32] The scanning electron microscopy (SEM) and transmission electron microscopy (TEM) images (Figures S7 and S8) show that the double-shell box structure is maintained during this exchange process. After surface coating with polydopamine and subsequent calcination, the carbon-coated double-shell bismuth hollow boxes (C@DSBC) are obtained and studied by SEM and TEM imaging analysis. As shown in Figures 1B and S9, the uniform cubic shape remains after coating and subsequent calcination. The TEM and scanning TEM (STEM) images (Figures 1C and S10) show a porous dual-shell structure of these boxes with the thickness of each shell estimated to be around several nanometers. The high-angle annular dark-field STEM (HAADF-STEM) image (Figure 1D) shows the lattice spacings of 0.33 nm and 0.30 nm with an interfacial angle of 56° indexed as (012) and (004) facets of bismuth, respectively. A combination of these data with

those of XRPD data shown in Figure 1E reveals that the composition in the as-prepared sample is mainly rhombohedral bismuth phase. Additionally, the STEM elemental mapping images (Figure 1F) illustrate the even distribution of bismuth, carbon, and nitrogen, indicating that the nitrogen-doped carbon homogeneously coats the surface of bismuth boxes. The N-doped nature of the carbon coating is also demonstrated by X-ray photoelectron spectroscopy (XPS) (Figures 1G, S11A, and S11B).[34,35] Furthermore, the Raman spectrum (Figure S12) shows that this carbon coating is highly amorphous, while the carbon content is around 7% according to the thermogravimetric analysis (Figure S13).[36–38]

The microsized bismuth is selected as the control sample to offer a more comprehensive understanding of the improved reversible capacity of nanostructured alloy anodes. The detailed characterizations are shown in Figure S14 (SEM image and XPS survey spectrum). As shown in Figure 2A, the C@DSBC sample achieves an initial reversible capacity of 351 mAh g^{-1} with an initial Coulombic efficiency of 52%. This low initial Coulombic efficiency can be attributed to the irreversible reaction of K^+ with Bi, the decomposition of electrolyte, and the formation of the solid electrolyte interface (SEI).[39,40] It is noteworthy that the initial Coulombic efficiency of microsized bismuth is 64%. The lower Coulombic efficiency of C@DSBC than in the case of microsized bismuth might originate from irreversible reactions between surface functional groups of the carbon coating and potassium as well as the reactions between residual bismuth sulfide and potassium, which are irreversible in this voltage range.[41,42] Despite the low initial Coulombic efficiency, the subsequent discharging/charging curves of C@DSBC exhibit good overlays, suggesting the good stability of the previously formed SEI, which benefits the subsequent cycling stability. Some slight differences between microsized bismuth and double-shell structure can be found in Figures 2A and 2B. The initial discharging curve for C@DSBC shows several plateaus. On the other hand, the discharging curve of microsized bismuth features one plateau. The cyclic voltammetry (CV) curves show only one significant reduction peak for microsized bismuth (Figure S15), while a much higher anodic current response can be observed before 0.25 V on the CV curves of C@DSBC (Figure 2C). This indicates that there are differences between C@DSBC and microsized bismuth samples during their initial cycling processes. After the initial cycles, as shown in Figure 2D, C@DSBC exhibited a good rate performance as an anode for potassium-ion batteries. Specifically, it delivered the reversible capacities of 340, 302, 274, 251, and 222 mAh g^{-1} under the current densities of 40, 80, 200, 400, and 800 mA g^{-1}, corresponding to 0.1, 0.2, 0.5, 1, and 2 C, respectively. By way of comparison, the rate performance of microsized bismuth is shown as Figure S16. Additionally, Table S1 shows a comparison of the samples studied with state-of-the-art materials. Regarding the long cycling durability, C@DSBC exhibited an enhanced durability compared with that of the microsized bismuth. Specifically, as shown in Figure 2E, during the initial period, both bismuth samples exhibited stable reversible specific capacities of around 300 mAh g^{-1}. After being cycled for around 20 cycles, a more significant decrease is observed for the reversible capacity of the microsized bismuth while the reversible capacity of C@DSBC remains over 300 mAh g^{-1}. After cycling for 200 cycles, the reversible capacity of the microsized bismuth is 65 mAh g^{-1}, corresponding to the capacity loss of 77.0% during 200 cycles. On the contrary, the reversible capacity of C@DSBC is maintained over 200 mAh g^{-1}, which corresponds to the capacity decay of 0.13% per cycle, showing a good durability of C@DSBC as an anode for potassium-ion batteries. Additionally, the SEM image (Figure S17) reveals that the cubic structure was maintained after cycling, suggesting the good durability of C@DSBC. Note that the main electrochemical reactions related to the storage potassium ions are the alloy

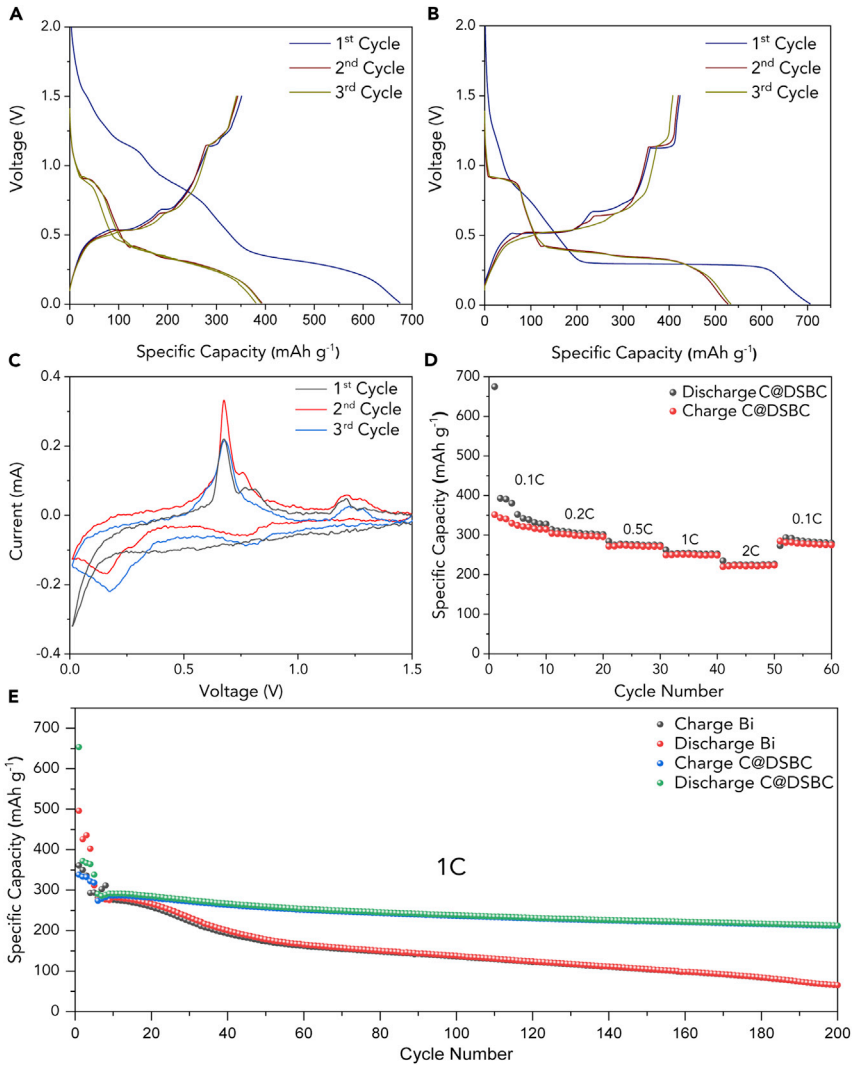

Figure 2. Electrochemical Performance of Bismuth Samples

(A and B) Initial cycling curves of (A) C@DSBC and (B) microsized bismuth.

(C) Initial CV curves of C@DSBC.

(D) Rate performance of C@DSBC.

(E) Long cycling performance of C@DSBC and microsized bismuth.

reactions between potassium and bismuth. The previous study on the lithiation of silicon suggests that the cracking and consequent peeling-off are the main reasons for capacity fading of alloying anodes.[9] Additionally, the first-principles DFT study indicates larger volume expansion upon alloying with potassium than upon alloying with sodium and lithium.[26] Therefore, the main reason for decreasing the reversible capacity of bismuth samples might be the repetitive volume expansion during the alloying/dealloying reactions. In regard to the comparison of long cycling performance of C@DSBC and microsized bismuth, it is noteworthy that the cycling durability of the C@DSBC sample is better than that of microsized bismuth. This enhanced durability might originate from the protective role of the carbon coating, which functions as a mechanical backbone to ensure that all bismuth is electrochemically active and limits the SEI formation on the outer surface instead of that on bismuth nanoparticles.[3]

The electrochemical characterization suggests that C@DSBC behaves differently from microsized bismuth during the initial cycling. The difference in electrochemical reactions during the cycling process shown by various synchrotron-based techniques reveals the origin of the improved capacity.

First, the cycling process of both C@DSBC and microsized bismuth under low current densities is monitored by *operando* XRPD. As previously reported, the electrochemical reaction of bismuth and potassium ion during the discharging process can be represented by the following equation:[39,40]

$$Bi \rightarrow KBi_2 \rightarrow K_3Bi_2 \rightarrow K_3Bi.$$

In our *operando* XRPD study, during the cycling process of double-shell bismuth and microsized bismuth, the most significant difference appears during transformation from K_3Bi_2 to K_3Bi. During the initial discharging process of double-shell bismuth, as shown in Figure 3A, the reflection peak is assigned to the $(11\bar{5})$ facet of K_3Bi_2, which is located at 18.18°, and appears for the discharging taking place at the voltage of around 0.3 V. With the progress of electrochemical alloying reaction, the intensity of reflection peak of K_3Bi_2 starts to decrease and the reflection peak almost disappears when the voltage approaches a value of 0.2 V. Subsequently, as shown in Figure 3C, when the intensity of reflection of K_3Bi_2 decreases, the (222) peak of K_3Bi, which is located at 12.16°, appears, indicating the K_3Bi_2 phase is going through a transformation to K_3Bi. When the charging process starts, the intensity of K_3Bi decreases significantly and the intensity of K_3Bi_2 increases subsequently and decreases afterward, indicating the superior reversibility of C@DSBC as an anode for potassium-ion batteries. As a comparison, the microsized bismuth was also subjected to the same process with the same current density. Interestingly, as shown in Figure 3B, the reflection of K_3Bi_2 appears around the middle of the discharging plateau. The intensity of this reflection peak only decreases partially with the proceeding electrochemical reaction. Afterward, at the initial stage of charging, the intensity of reflection for K_3Bi_2 only slightly decreases, indicating that most of the K_3Bi_2 remains unreacted and the reversibility of microsized bismuth is poor. More importantly, during the discharging process of bismuth, as shown in Figure 3D, the intensity of the K_3Bi phase is low. Compared with the high intensity of K_3Bi reflection peak in the case of C@DSBC, one can conclude that there is no significant formation of K_3Bi phase. Therefore, under the low current density, the main difference between the electrochemical reactions of these two materials is the transformation from K_3Bi_2 to K_3Bi. It is noteworthy that in addition to the visible difference between the initial and subsequent cycling curves, a similar trend in the intensity change of K_3Bi is observed on the plots of *operando* XRPD data for subsequent cycles of C@DSBC and microsized bismuth (see Figures S18 and S19). This result indicates that the electrochemical alloy reaction between C@DSBC and potassium is more complete than that between microsized bismuth and potassium. Initially, the main final product from the electrochemical reaction of C@DSBC is K_3Bi while the one in the case of microsized bismuth is K_3Bi_2. In previous reports, both Huang et al. and Lei et al. reported that the normalized volume expansion during the electrochemical reaction is over 400% from Bi to K_3Bi.[39,40] Combined with the data of the volume expansion from previous studies, as shown in the scheme of Figure 3E, this difference might come from the much higher strain and volume expansion during the phase-transformation process from K_3Bi_2 to K_3Bi. With the large internal voids, the C@DSBC sample is capable of accommodating larger volume expansion. On the contrary, the microsized bismuth can only tolerate smaller volume expansion, resulting in a change of electrochemical reaction path. Therefore, the final main

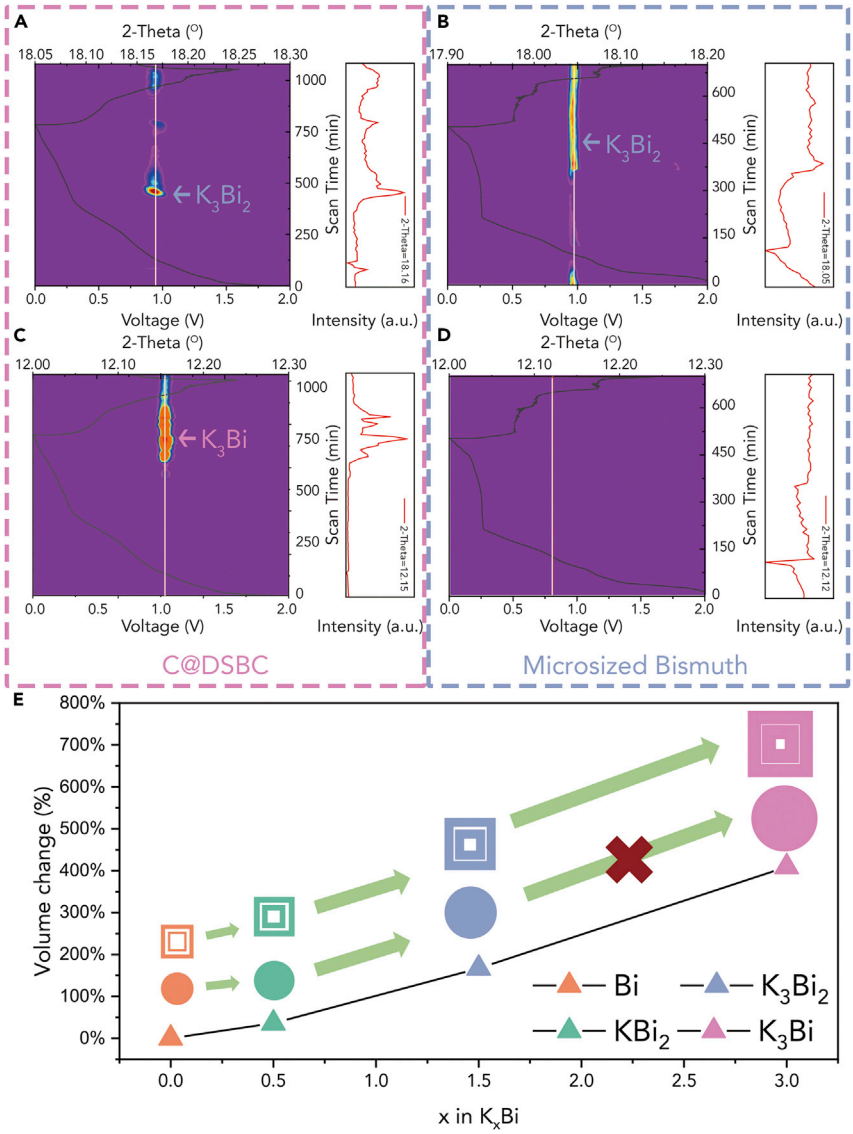

Figure 3. Origin of Superior Electrochemical Performance under Low Current Density

(A–D) Comparison of contour plots of the *operando* XRPD with superimposed voltage profiles shown for selected ranges of K_3Bi_2 (A and B) and K_3Bi (C and D).

(E) Scheme of superior electrochemical performance of C@DSBC under low current density.

product after initial electrochemical reaction of microsized bismuth is K_3Bi_2, corresponding to the volume expansion of around 167%. To sum up, nanostructured alloy anodes offer enhanced capability to accommodate large volume expansion, resulting in a more complete alloy reaction and consequent higher reversible capacity under low current density.

When the electrochemical reaction occurs under a relatively high current density, it might be quite different from that under low current density. The electrochemical reaction taking place on C@DSBC under high current density (2 C) is explored by combining *operando* XRPD and *ex situ* XANES. The *operando* XRPD reveals that the reflection intensity of bismuth in C@DSBC decreases significantly with the electrochemical process (Figure 4A). On the contrary, the reflection intensity observed

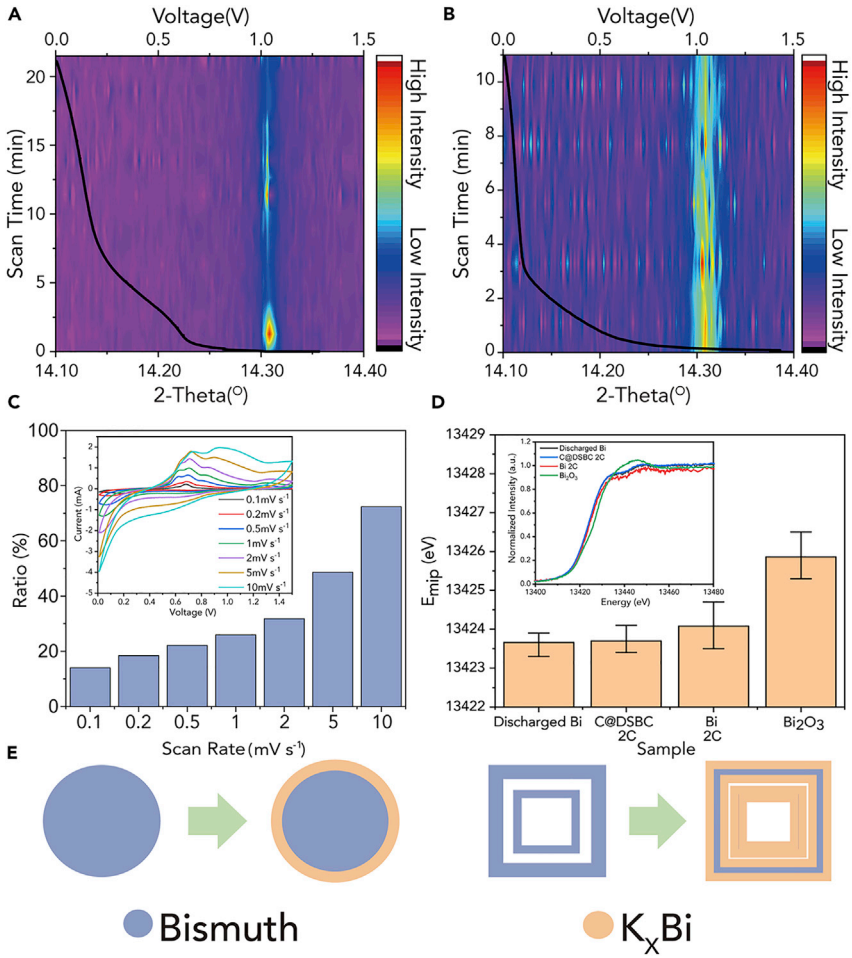

Figure 4. Origin of Superior Electrochemical Performance under High Current Density

(A and B) Comparison of contour plots of the *operando* XRPD with superimposed voltage profiles shown for bismuth reflection of different samples: C@DSBC (A) and microsized bismuth (B).

(C) The pseudocapacitive contribution obtained for C@DSBC (with inset showing the CV curves of C@DSBC at various sweep rates).

(D) The corresponding E_{mip} for various samples (with inset showing the XANES spectra of various samples; error bars represent the range of measured E_{mip}).

(E) Scheme illustrating the superior electrochemical performance of C@DSBC under high current density.

for microsized bismuth is only slightly reduced (Figure 4B), indicating that more bismuth in this sample remains unreacted. This finding demonstrates that the electrochemical alloying reaction of bismuth in C@DSBC with potassium is more complete than that in microsized bismuth. However, surprisingly, unlike the electrochemical process under low current density mentioned above, there is no significant change in the intensities of both K_3Bi_2 phase and K_3Bi phase (Figure S20) on the spectra of C@DSBC. This finding indicates that the main electrochemical reaction of C@DSBC under the relatively high current density could be a surface-driven adsorption reaction. This finding is also confirmed by the kinetics analysis of C@DSBC. As shown in Figure 4C, the contribution arising from pseudocapacitive behavior of double-shelled structured bismuth, which is calculated from the CV data for various sweep rates (Figure 4C, inset), increases to over 70% at the scan rate of 10 mV s^{-1}. This indicates that the main contribution to the reversible capacity might originate from the

surface-driven adsorption reactions rather than the alloying reaction with crystallized product mentioned above at the low current density. This might be the reason why no significant crystallized alloy of potassium and bismuth is detected by *operando* XRPD during cycling under a relatively high current density. Therefore, the *ex situ* XANES spectroscopy was employed to reveal the difference in electrochemical reaction products from both samples.

The microsized bismuth sample discharged to 0.01 V with potassium as the counter electrode under a low current density and bismuth oxide (Bi_2O_3) were selected as the standard samples. In the XANES spectra, the energy inflection point of the BiL_{III} edge indicates the average oxidation state of bismuth in the corresponding samples. On these *ex situ* spectra (Figure 4D, inset), the BiL_{III} edge of C@DSBC after discharging under the current density of 2 C is closer to that of the discharged Bi standard sample, compared with that of the discharged microsized bismuth. To illustrate this point clearly, the position of the main inflection point (E_{mip}) is selected as the descriptor of oxidation state of bismuth in the corresponding samples (Figure S21). As shown in the bar graph (Figure 4D), the bismuth in C@DSBC shows an average oxidation state, corresponding to E_{mip} of 13,423.7 eV, similar to that of the discharged Bi sample (13,423.66 eV), while the microsized bismuth sample shows a higher oxidation state (13,424.08 eV). As suggested by Figure 4E, this difference in the oxidation state might indicate that the electrochemical reaction under high current density is dominated by surface-driven adsorption reactions. The lower average oxidation state of C@DSBC indicates that its electrochemical reaction generates more alloy product, resulting in a lower average oxidation state. This might come from the higher surface area of 33.1 $m^2\ g^{-1}$ of C@DSBC as compared with 9.2 $m^2\ g^{-1}$ of microsized bismuth (Figure S22). Therefore, the nanostructured alloy anodes offer larger surface area and more electrochemical active sites to react with alkaline ions, resulting in larger consumption of electrode materials, lower average oxidation states, and, consequently, higher reversible capacities under high current density.[43]

Combination of the results from *operando* XRPD and *ex situ* XANES allows for two main conclusions. First, the improved reversible capacities of nanostructured alloy anodes in batteries under various current densities have different origins. For cycling under low current density, the key is a more complete alloy reaction resulting from the change in the electrochemical alloying reaction path. Under the condition of high current density, the surface-driven adsorption reactions are more important, which result in larger consumption of electrode materials and, consequently, a lower average oxidation state. Second, the key role of the nanostructure in enhancing the electrochemical performance of alloy anodes is identified. Specifically, the higher reversible capacity under low current density originates from the high capability of nanostructured alloy anode to accommodate larger volume expansion than that in the microsized sample. In the case of high current density, the higher reversible capacity originates from the larger surface area of nanostructured alloy anode, which offers more electrochemical active sites to react with alkali ions. In regard to comparison of the processes under high and low current densities, it is noteworthy that the process at high current densities is more sensitive to the surface area because the dominating electrochemical reactions in this circumstance are the surface-driven adsorption reactions. Regarding the process under low current densities, the phase-evolution reactions are the dominating electrochemical reactions, resulting in a larger volume expansion than that observed under high current density. Therefore, these results offer guidance for the rational design and engineering of alloy anodes for rocking-chair batteries. Specifically, enlarging the surface area is more

critical for the alloy anodes applied in the scenarios, which require fast discharging/charging. However, in relation to the scenarios at low current density, the ability to tolerate the volume expansion is more important. These conclusions can serve as guidance for the rational design and engineering of alloy anodes for rocking-chair batteries.

Conclusions

In summary, we have constructed new dual-shell structured bismuth boxes as anodes for potassium-ion batteries. Combining several synchrotron-based techniques and employing dual-shell bismuth boxes permitted us to reveal the origins of the improved reversible capacity of nanostructured alloy anodes under various current densities. The origin under low current density is the change of electrochemical reaction path, which is derived from the enhanced capability of nanostructured anode to tolerate the larger volume expansion. Under high current density, the origin of this improvement is associated with surface-driven electrochemical reactions promoted by the larger surface area of nanostructured anodes. This finding offers guidance for the rational design and engineering of electrodes for various applications.

EXPERIMENTAL PROCEDURES

Synthesis of Materials

Synthesis of ZIF-8 Cubes

First, 55 mg of zinc acetate dihydrate, 8 mg of hexadecyl trimethyl ammonium bromide (CTAB), and 1.14 g of 2-methylimidazole were dissolved in 80 mL of deionized water.[28] Next, the resulting solution was mixed and stirred for 5 min at room temperature. The as-prepared mixed solution was transferred into a Teflon-lined autoclave and placed in a 120°C oven for 6 h. After synthesis, the sample was washed three times with deionized water and ethanol and dried at 60°C overnight.

Synthesis of C@DSBC

Forty milligrams of the as-prepared ZIF-8 was transferred into a round-bottomed flask and dispersed in 30 mL of anhydrous ethanol under ultrasonication for 10 min. The flask was soaked in an 80°C oil bath. Thereafter, a mixed solution containing 0.54 g of thioacetamide and 10 mL of anhydrous ethanol was added into the flask and the reaction was processed at 80°C for 0.5 h. The intermediate was collected by centrifugation and washed twice with anhydrous ethanol. Next, the as-prepared sample was redispersed in 20 mL of acetone while another solution was prepared by dissolving 0.1 g of bismuth chloride in 20 mL of acetone. The former solution was poured into the latter one under magnetic stirring, which was stopped after 3 h. The product was collected and washed three times with acetone and ethanol. The as-prepared sample was then redispersed in a solution containing 40 mg of Trizma Base and 30 mL of distilled water. Finally, 6 mg of dopamine hydrochloride was added rapidly into the suspension under intense stirring. The product was washed with ethanol and collected by centrifugation after a 3-h reaction at room temperature. The resulting sample was dried overnight in a vacuum oven and calcined in a tube furnace at 400°C for 3 h with a ramping rate of 3°C per minute.

Materials Characterization

XRPD data were collected on Rigaku MiniFlex 600 X-ray diffractometer. The field-emission SEM images were acquired by an FEI Quanta 450 FEG scanning electron microscope. The TEM images were taken by an FEI Tecnai G2 Spirit. The STEM and HAADF-STEM images were taken by an FEI Titan Themis. The *operando*

XRPD was conducted in the powder diffraction beamline of the Australian Synchrotron (ANSTO) with a beamline wavelength of 0.5904 Å in transmission mode. The coin cells for *operando* powder diffraction are modified from C2032 coin cells with X-ray transparent windows made from Kapton film.[18] The *ex situ* XANES spectra were collected in the X-ray absorption spectroscopy (XAS) beamline of ANSTO. The electrodes tested in XAS were taken from disassembled coin cells and sealed by Kapton tape in an Argon-filled glovebox. The electrodes were tested in fluorescence mode. The discharged bismuth sample was prepared in a coin cell using microsized bismuth and potassium as the cathode and anode, respectively. The coin cell was discharged to 0.01 V under a current density of 0.05 C. The surface area was evaluated from nitrogen adsorption data measured at 77.3 K (ASAP 2020) using the Brunauer-Emmett-Teller method. XPS measurements were conducted on the X-ray microprobe of a Thermo Escalab 250Xi with monochromatic Al Kα radiation.

Electrochemical Measurements

The electrochemical performance tests were carried out in C2032 coin cells at room temperature. The working electrode consisted of active material (i.e., dual-shell bismuth and pristine bismuth), carbon black (Super P from VWR, supplied by Alfa Aesar), and binder (sodium carboxymethylcellulose, average molecular weight ~700,000, Sigma-Aldrich) using a weight ratio of 60:30:10, while the copper foil was employed as the current collector. The electrolyte was composed of 2.0 M potassium bis(fluorosulfonyl)imide dissolved in 1,2-dimethoxyethane. Galvanostatic tests were performed on a Landt CT2001A battery testing system. The CV data were collected on a Gamry 1000e electrochemical station.

SUPPLEMENTAL INFORMATION

Supplemental Information can be found online at https://doi.org/10.1016/j.matt.2019.07.006.

ACKNOWLEDGMENTS

This work was supported financially by the Australian Research Council through Discovery and Linkage Project programs (DP160104866, DP170104464, LP160100927, DE150101234, and FL170100154). This research was undertaken on the powder diffraction and XAS beamlines at the Australian Synchrotron, part of ANSTO. We acknowledge Dr. Ashley Slattery, from the AMMRF facility at the University of Adelaide, for microscopy services.

AUTHOR CONTRIBUTIONS

F.X., L.Z., B.C., and D.C. designed the synthesis procedure and conducted all the electrochemical performance tests. F.X. and Q.G. carried out the *operando* XRPD. F.X. and B.J. carried out the *ex situ* XANES. S.Q. supervised the project and co-wrote the manuscript. All authors discussed the results and contributed to writing the manuscript. All authors have approved the final version of the manuscript.

DECLARATION OF INTERESTS

The authors declare no competing interests.

Received: May 8, 2019
Revised: June 18, 2019
Accepted: July 12, 2019
Published: September 18, 2019

REFERENCES

1. Wang, M., Jiang, C., Zhang, S., Song, X., Tang, Y., and Cheng, H.M. (2018). Reversible calcium alloying enables a practical room-temperature rechargeable calcium-ion battery with a high discharge voltage. Nat. Chem. *10*, 667–672.
2. Li, Y., Yan, K., Lee, H.-W., Lu, Z., Liu, N., and Cui, Y. (2016). Growth of conformal graphene cages on micrometre-sized silicon particles as stable battery anodes. Nat. Energy *1*, 15029.
3. Liu, N., Lu, Z., Zhao, J., McDowell, M.T., Lee, H.W., Zhao, W., and Cui, Y. (2014). A pomegranate-inspired nanoscale design for large-volume-change lithium battery anodes. Nat. Nanotechnol. *9*, 187–192.
4. Sun, J., Lee, H.W., Pasta, M., Yuan, H.T., Zheng, G.Y., Sun, Y.M., Li, Y.Z., and Cui, Y. (2015). A phosphorene-graphene hybrid material as a high-capacity anode for sodium-ion batteries. Nat. Nanotechnol. *10*, 980–985.
5. Sultana, I., Rahman, M.M., Chen, Y., and Glushenkov, A.M. (2018). Potassium-ion battery anode materials operating through the alloying-dealloying reaction mechanism. Adv. Funct. Mater. *28*, 1703857.
6. Lao, M., Zhang, Y., Luo, W., Yan, Q., Sun, W., and Dou, S.X. (2017). Alloy-based anode materials toward advanced sodium-ion batteries. Adv. Mater. *29*, 1700622.
7. Obrovac, M.N., and Chevrier, V.L. (2014). Alloy negative electrodes for Li-ion batteries. Chem. Rev. *114*, 11444–11502.
8. Yang, Z., Zhang, J., Kintner-Meyer, M.C.W., Lu, X., Choi, D., Lemmon, J.P., and Liu, J. (2011). Electrochemical energy storage for green grid. Chem. Rev. *111*, 3577–3613.
9. Sun, Y.M., Liu, N.A., and Cui, Y. (2016). Promises and challenges of nanomaterials for lithium-based rechargeable batteries. Nat. Energy *1*, 16071.
10. Jian, Z., Luo, W., and Ji, X. (2015). Carbon electrodes for K-ion batteries. J. Am. Chem. Soc. *137*, 11566–11569.
11. Zhang, W.C., Mao, J.F., Li, S.A., Chen, Z.X., and Guo, Z.P. (2017). Phosphorus-based alloy materials for advanced potassium-ion battery anode. J. Am. Chem. Soc. *139*, 3316–3319.
12. Zhang, W.C., Liu, Y.J., and Guo, Z.P. (2019). Approaching high-performance potassium-ion batteries via advanced design strategies and engineering. Sci. Adv. *5*, eaav7412.
13. Hatchard, T.D., and Dahn, J.R. (2004). In situ XRD and electrochemical study of the reaction of lithium with amorphous silicon. J. Electrochem. Soc. *151*, A838–A842.
14. Wang, F., Wu, L., Key, B., Yang, X.Q., Grey, C.P., Zhu, Y., and Graetz, J. (2013). Electrochemical reaction of lithium with nanostructured silicon anodes: a study by in-situ synchrotron X-ray diffraction and electron energy-loss spectroscopy. Adv. Energy Mater. *3*, 1324–1331.
15. Sottmann, J., Herrmann, M., Vajeeston, P., Hu, Y., Ruud, A., Drathen, C., Emerich, H., Fjellvåg, H., and Wragg, D.S. (2016). How crystallite size controls the reaction path in nonaqueous metal ion batteries: the example of sodium bismuth alloying. Chem. Mater. *28*, 2750–2756.
16. Cook, J.B., Lin, T.C., Kim, H.S., Siordia, A., Dunn, B.S., and Tolbert, S.H. (2019). Suppression of electrochemically driven phase transitions in nanostructured MoS_2 pseudocapacitors probed using operando X-ray diffraction. ACS Nano *13*, 1223–1231.
17. Lu, J., Wu, T.P., and Amine, K. (2017). State-of-the-art characterization techniques for advanced lithium-ion batteries. Nat. Energy *2*, 17011.
18. Lin, F., Liu, Y., Yu, X., Cheng, L., Singer, A., Shpyrko, O.G., Xin, H.L., Tamura, N., Tian, C., Weng, T.C., et al. (2017). Synchrotron X-ray analytical techniques for studying materials electrochemistry in rechargeable batteries. Chem. Rev. *117*, 13123–13186.
19. Gu, Q., Kimpton, J.A., Brand, H.E.A., Wang, Z., and Chou, S. (2017). Solving key challenges in battery research using in situ synchrotron and neutron techniques. Adv. Energy Mater. *7*, 1602831.
20. Bak, S.M., Shadike, Z., Lin, R., Yu, X., and Yang, X.Q. (2018). In situ/operando synchrotron-based X-ray techniques for lithium-ion battery research. NPG Asia Mater. *10*, 563–580.
21. Xu, X., Zhao, R., Chen, B., Wu, L., Zou, C., Ai, W., Zhang, H., Huang, W., and Yu, T. (2019). Progressively exposing active facets of 2D nanosheets toward enhanced pseudocapacitive response and high-rate sodium storage. Adv. Mater. *31*, 1900526.
22. Chao, D., Liang, P., Chen, Z., Bai, L., Shen, H., Liu, X., Xia, X., Zhao, Y., Savilov, S.V., Lin, J., et al. (2016). Pseudocapacitive Na-ion storage boosts high rate and areal capacity of self-branched 2D layered metal chalcogenide nanoarrays. ACS Nano *10*, 10211–10219.
23. Chao, D., Ouyang, B., Liang, P., Huong, T.T.T., Jia, G., Huang, H., Xia, X., Rawat, R.S., and Fan, H.J. (2018). C-plasma of hierarchical graphene survives SnS bundles for ultrastable and high volumetric Na-ion storage. Adv. Mater. *30*, 1804833.
24. Chao, D., Zhu, C., Yang, P., Xia, X., Liu, J., Wang, J., Fan, X., Savilov, S.V., Lin, J., Fan, H.J., et al. (2016). Array of nanosheets render ultrafast and high-capacity Na-ion storage by tunable pseudocapacitance. Nat. Commun. *7*, 12122.
25. Son, Y., Ma, J., Kim, N., Lee, T., Lee, Y., Sung, J., Choi, S.H., Nam, G., Cho, H., Yoo, Y., et al. (2019). Quantification of pseudocapacitive contribution in nanocage-shaped silicon–carbon composite anode. Adv. Energy Mater. *9*, 1803480.
26. Kim, H., Kim, J.C., Bianchini, M., Seo, D.-H., Rodriguez-Garcia, J., and Ceder, G. (2018). Recent progress and perspective in electrode materials for K-ion batteries. Adv. Energy Mater. *8*, 1702384.
27. Hwang, J.Y., Myung, S.T., and Sun, Y.K. (2018). Recent progress in rechargeable potassium batteries. Adv. Funct. Mater. *28*, 1802938.
28. Pan, Y., Heryadi, D., Zhou, F., Zhao, L., Lestari, G., Su, H., and Lai, Z. (2011). Tuning the crystal morphology and size of zeolitic imidazolate framework-8 in aqueous solution by surfactants. CrystEngComm *13*, 6937–6940.
29. Zhang, P., Guan, B.Y., Yu, L., and Lou, X.W. (2018). Facile synthesis of multi-shelled ZnS-CdS cages with enhanced photoelectrochemical performance for solar energy conversion. Chem *4*, 162–173.
30. Fang, Y.J., Yu, X.Y., and Lou, X.W. (2018). Formation of polypyrrole-coated Sb_2Se_3 microclips with enhanced sodium-storage properties. Angew. Chem. Int. Ed. *57*, 9859–9863.
31. Fang, Y.J., Yu, X.Y., and Lou, X.W. (2019). Bullet-like Cu_9S_5 hollow particles coated with nitrogen-doped carbon for sodium-ion batteries. Angew. Chem. Int. Ed. *58*, 7744–7748.
32. Xie, F., Zhang, L., Gu, Q., Chao, D., Jaroniec, M., and Qiao, S.Z. (2019). Multi-shell hollow structured Sb_2S_3 for sodium-ion batteries with enhanced energy density. Nano Energy *60*, 591–599.
33. Wu, H.B., and Lou, X.W. (2017). Metal-organic frameworks and their derived materials for electrochemical energy storage and conversion: promises and challenges. Sci. Adv. *3*, eaap9252.
34. Xie, F., Zhang, L., Su, D., Jaroniec, M., and Qiao, S.Z. (2017). $Na_2Ti_3O_7$@N-doped carbon hollow spheres for sodium-ion batteries with excellent rate performance. Adv. Mater. *29*, 1700989.
35. Zangmeister, R.A., Morris, T.A., and Tarlov, M.J. (2013). Characterization of polydopamine thin films deposited at short times by autoxidation of dopamine. Langmuir *29*, 8619–8628.
36. Chen, S., Duan, J., Ran, J., Jaroniec, M., and Qiao, S.Z. (2013). N-doped graphene film-confined nickel nanoparticles as a highly efficient three-dimensional oxygen evolution electrocatalyst. Energy Environ. Sci. *6*, 3693–3699.
37. Ferrari, A.C., and Basko, D.M. (2013). Raman spectroscopy as a versatile tool for studying the properties of graphene. Nat. Nanotechnol. *8*, 235–246.
38. Ferrari, A.C., and Robertson, J. (2000). Interpretation of Raman spectra of disordered and amorphous carbon. Phys. Rev. B *61*, 14095–14107.
39. Huang, J.Q., Lin, X.Y., Tan, H., and Zhang, B. (2018). Bismuth microparticles as advanced anodes for potassium-ion battery. Adv. Energy Mater. *8*, 1703496.
40. Lei, K.X., Wang, C.C., Liu, L.J., Luo, Y.W., Mu, C.N., Li, F.J., and Chen, J. (2018). A porous network of bismuth used as the anode material for high-energy-density potassium-ion batteries. Angew. Chem. Int. Ed. *57*, 4687–4691.

41. Gao, H., Zhou, T.F., Zheng, Y., Zhang, Q., Liu, Y.Q., Chen, J., Liu, H.K., and Guo, Z.P. (2017). CoS quantum dot nanoclusters for high-energy potassium-ion batteries. Adv. Funct. Mater. *27*, 1702634.

42. Zeng, C., Xie, F., Yang, X.F., Jaroniec, M., Zhang, L., and Qiao, S.Z. (2018). Ultrathin titanate nanosheets/graphene films derived from confined transformation for excellent Na/K ion storage. Angew. Chem. Int. Ed. *57*, 8540–8544.

43. Wang, J., Wan, J., and Wang, D. (2019). Hollow multishelled structures for promising applications: understanding the structure–performance correlation. Acc. Chem. Res. *52*, 2169–2178.